RSC Advances

PAPER

View Article Online
View Journal | View Issue

Cite this: *RSC Adv.*, 2026, **16**, 22610

Tunable anti-biofilm activity of Zn-doped CuO nanoparticles: structural, morphological, and biological insights against Gram-positive and Gram-negative bacteria

N. Khlifi, *[ac] S. Mnif,[b] C. Zerrouki,[c] H. Guermazi,[a] N. Fourati,[c] Benoît Duponchel,[d] S. Aifa[b] and S. Guermazi[a]

Received 4th March 2026
Accepted 25th April 2026

DOI: 10.1039/d6ra01884j

rsc.li/rsc-advances

Biofilm-associated infections represent a major challenge in healthcare due to antibiotic resistance, driving the search for effective nano-antimicrobial agents. This study presents the synthesis of Zn-doped CuO nanoparticles ($Cu_{1-x}Zn_xO$, $0 \leq x \leq 0.5$) *via* an eco-friendly co-precipitation method and investigates their anti-adhesive efficacy against Gram-positive *Staphylococcus epidermidis* S61 and Gram-negative *Pseudomonas aeruginosa* 2629. Comprehensive characterization (XRD, SEM, AFM, FTIR, and EDX) revealed that Zn doping refined crystallite size, altered surface morphology, and enhanced specific surface area. The anti-biofilm assays demonstrated that Zn incorporation significantly improved anti-adhesive activity against *S. epidermidis*, with $x = 0.2$ achieving >73% inhibition at 500 μg mL^{-1}. In contrast, pure CuO was most effective against *P. aeruginosa*, indicating a strain-dependent response linked to bacterial cell-wall structure. The anti-adhesive mechanism is attributed to nanoparticle-surface interactions, ion release, and reactive oxygen species generation. These findings highlight the potential of compositionally tunable Zn-doped CuO nanoparticles as selective anti-biofilm agents for combating healthcare-associated infections.

1 Introduction

The increasing prevalence of biofilm-associated infections in healthcare and industrial settings represents a significant challenge to global health, largely due to the rise in antibiotic-resistant bacterial strains.[1,2] Bacterial biofilms, which are structured communities of microorganisms embedded in a self-produced extracellular polymeric matrix, are inherently resistant to conventional antimicrobial therapies and are a leading cause of persistent and chronic infections.[3–5] Pathogens such as *Staphylococcus epidermidis* (a Gram-positive bacterium) and *Pseudomonas aeruginosa* (a Gram-negative bacterium) are particularly notorious for forming resilient biofilms on medical implants and surfaces, leading to costly and difficult-to-treat nosocomial infections.[6,7]

Inorganic metal oxide nanoparticles (MO-NPs) have emerged as a promising alternative to conventional antibiotics due to their broad-spectrum antimicrobial activity, lower propensity for inducing resistance, and multifunctional properties.[8,9] Among these, copper oxide (CuO) and zinc oxide (ZnO) have attracted considerable attention. CuO is a p-type semiconductor with a narrow band gap (1.2 eV), known for its catalytic, electronic, and antibacterial properties.[10] ZnO, an n-type semiconductor, is widely studied for its optical activity and strong antibacterial efficacy, often attributed to reactive oxygen species (ROS) generation.[11] Both oxides are cost-effective, environmentally benign, and exhibit potent activity against a range of pathogens.[12]

Doping CuO with transition metal ions, such as Zn^{2+}, is a well-established strategy to modulate its electronic structure, defect chemistry, and surface properties, thereby enhancing its functional performance.[13,14] The comparable ionic radii of Zn^{2+} (0.074 nm) and Cu^{2+} (0.073 nm) facilitate the substitutional incorporation of Zn into the CuO lattice, which can alter its optical, magnetic, and catalytic behavior.[15,16] Recent studies have shown that Zn doping can significantly influence the antibacterial and photocatalytic activities of CuO.[17,18] For instance, Thakur *et al.* reported that (Ag, Zn) co-doped CuO NPs exhibit enhanced bactericidal properties.[17] Similarly, Uthra *et al.* demonstrated improved antibiofilm activity of Zn-doped

[a]*Laboratory of Materials for Energy and Environment, and Modeling (LMEEM), Faculty of Sciences, University of Sfax, B.P: 1171, 3038, Tunisia. E-mail: khlifinadia1991@gmail.com*

[b]*Laboratory of Molecular and Cellular Screening Processes, Centre of Biotechnology of Sfax, P.O. Box 1177, 3018 Sfax, Tunisia*

[c]*Laboratory of Information and Energy Technology Systems and Applications (SATIE), UMR 8029, CNRS, ENS Paris-Saclay, CNAM, 292 Rue Saint-Martin, 7503 Paris, France*

[d]*Units of Dynamic and Structure of Molecular Materials (UDSMM), Littoral Côte-d'Opale University, France*

CuO against *Streptococcus mutans* compared to pure CuO.[18] Furthermore, recent advances have highlighted the potential of hybrid metal/metal oxide systems for enhanced antibacterial and antibiofilm applications, where the synergistic effects of combined materials and comprehensive characterization are crucial for understanding structure–activity relationships.[19,20]

However, despite these advances, a systematic and comparative investigation correlating the degree of Zn doping in CuO with its physicochemical properties and, more importantly, its strain-specific anti-adhesive efficacy against both Gram-positive and Gram-negative biofilm-forming bacteria remains largely unexplored. Most existing studies either focus on the antibacterial activity of pure or singly doped oxides[21,22] or lack a comprehensive suite of characterization techniques to convincingly link structural modifications to biological outcomes.[23,24] Furthermore, the differential response of Gram-positive and Gram-negative bacteria, which possess fundamentally different cell-wall architectures, to doped metal oxide nanoparticles is not well understood and is critical for designing targeted antimicrobial strategies.[25,26]

To address these gaps, this study presents a holistic investigation of Zn-doped copper oxide ($Cu_{1-x}Zn_xO$, $0 \leq x \leq 0.5$) nanoparticles synthesized *via* a simple and scalable co-precipitation method. We employ a multi-technique characterization approach, including X-ray diffraction (XRD), scanning electron microscopy (SEM), atomic force microscopy (AFM), Fourier transform infrared (FTIR) spectroscopy, and energy-dispersive X-ray (EDX) analysis to elucidate how Zn concentration influences crystallinity, morphology, elemental composition, and surface chemistry. Subsequently, we rigorously evaluate the anti-adhesive activity of these nanomaterials against two clinically relevant biofilm-forming models: *S. epidermidis* S61 (Gram-positive) and *P. aeruginosa* 2629 (Gram-negative).

We hypothesize that controlled Zn doping will selectively tune the anti-biofilm properties of CuO nanoparticles in a bacteria-specific manner, driven by doping-induced changes in surface area, crystal defects, and ion release kinetics. By establishing clear structure–property–activity relationships, this work aims to provide fundamental insights and a practical framework for engineering compositionally tunable metal oxide nanomaterials for effective biofilm prevention and control.

2 Experimental details and materials

2.1 Materials and synthesis

$Cu_{1-x}Zn_xO$ samples with varying compositions ($0 \leq x \leq 0.5$) were synthesized using the co-precipitation method. The synthesis procedure involved adding 1 M copper(II) sulfate pentahydrate ($CuSO_4 \cdot 5H_2O$) to 100 mL of distilled water and stirring the mixture for 15 minutes until homogeneous. Specific amounts of zinc chloride ($ZnCl_2$) were then added to the suspension. The precursor components were completely dissolved, and 10 mL of 2 M sodium hydroxide (NaOH) was added dropwise every 15 minutes to maintain a pH level between 11 and 12. The mixture was continuously stirred using a magnetic stirrer for 3 hours. The resulting precipitate was washed multiple times with a mixture of distilled water and ethanol to remove any residual impurities. Finally, the precipitate was dried at 80 °C for 12 hours and calcined at 500 °C for 4 hours to obtain the $Cu_{1-x}Zn_xO$ samples.

2.2 Anti-biofilm activity (anti-adhesive activity)

The anti-biofilm activities of $Cu_{1-x}Zn_xO$ ($0 \leq x \leq 0.5$) samples were performed against *S. epidermidis* S61 and *P. aeruginosa* 2629, two biofilm-forming strains from our laboratory collection.[27] Anti-adherence activities were tested in 96-well flat-bottom microtiter plates as described by Nostro *et al.*,[28] with some modifications. Nanoparticle solutions ($Cu_{1-x}Zn_xO$), dissolved in Tryptone Soy Broth (TSB) or Luria Bertani (LB) liquid medium, were subjected to an ultrasonic bath for 1 h at 25 °C. Solutions (100 μL) were then added into the first column of plates and used to perform a serial two-fold dilution. The addition of 50 μL of glucose at a final concentration of 2.25% in each well was performed only with TSB medium used for the development of *S. epidermidis* S61 biofilm. An overnight culture of *S. epidermidis* S61 was performed in TSB medium at 30 °C and diluted with TSB. 50 μL of bacterial suspension were used to inoculate all wells to reach a final absorbance of 0.1 at a wavelength of 600 nm. The culture of *P. aeruginosa* 2629 was performed in LB medium at 37 °C and diluted with LB. 50 μL of bacterial suspension were also used to inoculate all wells, reaching a final absorbance (600 nm) of 0.1. Cell culture without NPs served as a control. Following incubation for 24 h at 30 °C or 37 °C, TSB, LB, and planktonic cells were discarded by reversing the plate, and all wells were washed twice with 200 μL of sterile phosphate-buffered saline (PBS) (pH 7.2). These plates were then dried at 60 °C for 1 h. Each well was stained with 150 μL of 0.2% (w/v in 20% ethanol) crystal violet for 15 min. The well contents were removed, and the remaining crystal violet, which stained the attached bacteria, was rinsed thrice with water. A volume of 200 μL of 33% (v/v) glacial acetic acid was added to all wells, and the solubilization of biofilm was obtained following incubation for 1 h at room temperature. Finally, the optical density was measured with a microplate reader at a wavelength of 570 nm. Percentage of biofilm inhibition was calculated by comparing the absorbance of untreated and treated biofilms according to the following formula:

$$\text{Biofilm inhibition}(\%) = \frac{(\text{OD}_{\text{control}} - \text{OD}_{\text{treated}})}{\text{OD}_{\text{control}}} \times 100 \quad (1)$$

All experiments were performed in triplicate to obtain statistical confidence. The experimental data were presented as mean ± standard deviation. The statistical analysis was carried out through one-way and two-way analysis of variance (ANOVA) as well as Duncan's post hoc test using GraphPad Prism version 9 and Excel.

2.3 Characterization techniques

Prior to initiating anti-biofilm studies, a comprehensive analysis of the physical and chemical attributes of the prepared

samples was conducted, including their crystalline structure, phase purity, morphology, elemental composition, surface topography, and functional group chemistry. Powder X-ray diffraction (XRD) was performed using a D8 Advance Bruker diffractometer equipped with a Lynxeye detector, employing Cu Kα radiation ($\lambda = 1.5406$ Å) at 40 kV and 40 mA. Diffraction patterns were recorded over a 2θ range of 5–70° with a step size of 0.02° and a scanning rate of 0.2° per minute. The 2-Theta peak position accuracy of the utilized system is assumed to be better than ±0.007° across the full angular range, referencing NIST Standard Reference Material 1976. Regarding peak intensity uncertainties, these are sufficiently minimal to obviate the need for repeated measurements. This precision is achieved through a deliberately low scan speed of 0.2° per minute, which allows a high counting rate and thereby statistically reduces associated uncertainties (these uncertainties being proportional to the square root of the counting rate). The resulting data were used to identify crystal phases and estimate crystallite size *via* the Scherrer equation. Scanning electron microscopy (SEM, Hitachi S-3400 N, Japan) coupled with energy-dispersive X-ray spectroscopy (EDX) was utilized for morphological examination and elemental analysis. SEM images were acquired at an acceleration voltage of 20 kV to assess surface morphology and particle size distribution, while EDX provided semi-quantitative elemental composition with uncertainties. The latter is estimated at three different locations in the explored area to obtain an assessment of the dispersion of the proportions of the constituent chemical elements. The ratios will thus be expressed based on the average values and the uncertainties through the experimental standard deviations. Atomic force microscopy (AFM) was employed to investigate the surface morphology, roughness, and nanoscale morphological features. AFM imaging was conducted in tapping phase contrast mode using a Nanosurf easy Scan 2 Flex system. The used cantilevers were Super Sharp Silicon probes (from Nanosensors, Switzerland) with of about 190 kHz resonance frequency. The probe–surface distance is controlled with a precision better than 0.1 nm. Furthermore, both software and hardware improvements of the device controller (C3000 Controller) enable accurate interpolation, thereby electronically enhancing the overall precision. In addition, the sampling is presently sufficiently dense (at least one million data points) such that uncertainties due to statistical errors are well below 0.1 nm. Nevertheless, we have chosen to assign an uncertainty of ±0.1 nm to all raw data. The recorded images enabled determination of all roughness parameters, then extraction of particle dimension and size distribution, offering insights into nanoscale surface properties that may influence biofilm adhesion. Finally, Fourier transform infrared (FTIR) spectroscopy was performed using a Bruker spectrophotometer over the wavenumber range of 4000–400 cm^{-1}, with a resolution of 2 cm^{-1}. A background spectrum was recorded before each sample measurement and was used for correction. This technique allowed identification of characteristic vibrational modes corresponding to metal–oxygen bonds and other functional groups present on the nanoparticle surfaces.

3 Results and discussion

3.1 XRD structural analysis and phase identification

Powder X-ray diffraction (XRD) was employed to investigate the crystal structure and phase evolution of the synthesized $Cu_{1-x}Zn_xO$ NPs with varying Zn content ($x = 0$, 0.05, 0.1, 0.2, 0.3, 0.4, 0.5). The XRD patterns, presented in Fig. 1, were indexed and analyzed using X'Pert High Score software with reference to ICDD databases.

The diffraction pattern of the undoped CuO sample ($x = 0$) exhibits characteristic peaks at $2\theta = 32.02°$, 35.37°, 38.60°, 48.66°, 53.32°, 58.15°, 61.39°, 66.11°, and 67.91°, corresponding respectively to the (110), (002), (111), (−202), (020), (202), (−113), (−311), and (113) planes of monoclinic tenorite phase (ICDD card no. 01-089-2529, space group $C2/c$).[29,30] No secondary phases such as Cu_2O or $Cu(OH)_2$ were detected, confirming the high purity of the synthesized CuO.

For low Zn doping levels ($x = 0.05$), the XRD pattern remains similar to that of pure CuO, with no additional peaks attributable to ZnO or other zinc-containing phases. This suggests that Zn^{2+} ions (ionic radius 0.074 nm) were successfully incorporated into the CuO lattice, substituting for Cu^{2+} ions (0.073 nm) without inducing significant structural distortion, likely due to their comparable ionic sizes.[15,31]

At higher Zn concentrations ($x \geq 0.1$), additional diffraction peaks appear at $2\theta \approx 31.66°$, 34.25°, 36.07°, 47.36°, 56.50°, 62.70°, 65.95°, and 67.72°, which can be indexed to the (100), (002), (101), (102), (110), (103), (200), and (111) planes of hexagonal wurtzite ZnO (ICDD card no. 00-036-1451), as highlighted in the magnified views (Fig. 1b and c). This confirms the formation of a biphasic CuO/ZnO nanocomposite at higher doping levels. The coexistence of both phases without intermediate compounds suggests that Zn doping promotes phase separation rather than the formation of a continuous solid solution across the entire composition range.[32]

The lattice parameters a, b, c, β, and unit cell volume (V) for the monoclinic CuO phase were calculated using the eqn (2) and (3).[33,34] By considering a slightly overestimated angular uncertainty of 0.01° (the quadratic sum of the instrumental and experimental components), we can proceed with the uncertainty propagation law to determine the associated uncertainties for the different crystallographic parameters. Note that it is possible to adopt semiautomatic or automatic methods, based on a global adjustment of error propagation *via* the covariance matrix or through Rietveld refinement.

$$\frac{1}{{d_{hkl}}^2} = \frac{1}{\sin^2\beta}\left(\frac{h^2}{a^2} + \frac{k^2\sin^2\beta}{b^2} + \frac{l^2}{c^2} - \frac{2hl\cos\beta}{ac}\right) \quad (2)$$

$$V = abc\sin\beta \quad (3)$$

where d_{hkl} is the inter-planar spacing calculated from Bragg's law, and h, k, and l are Miller indices. The calculated crystallographic parameters and their respective uncertainties are summarized in Table 1. A gradual decrease in the lattice parameter a and V of CuO is observed with increasing x, suggesting lattice contraction due to Zn^{2+} substitution. This lattice

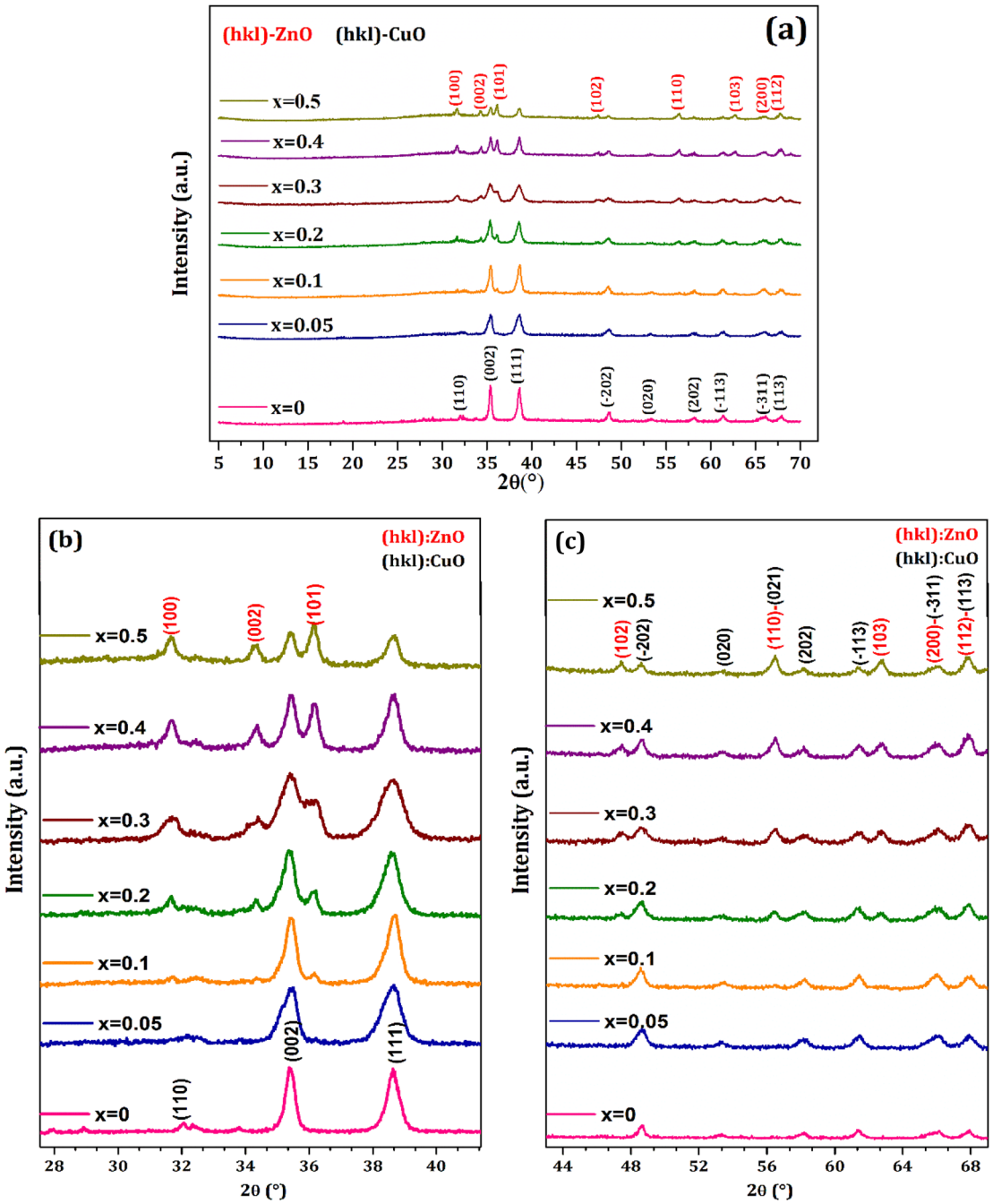

Fig. 1 (a) XRD pattern of $Cu_{1-x}Zn_xO$ ($0 \leq x \leq 0.5$) samples. (b and c) Enlarged view of the main peaks showing shifts in peak position and changes in peak broadening.

contraction indicates an increase in the material's density and a potential alteration in its electronic band structure, which can influence its surface reactivity and ion release kinetics, key factors in antibacterial activity.[35] For the ZnO phase, the parameters remain consistent with the standard wurtzite structure, confirming the formation of a well-crystallized secondary phase.

According to the International Tables for crystallography, CuO crystallizes in the monoclinic space group $C2/c$, with lattice parameters approximately equal to $a = 4.6837$ Å, $b = 3.4226$ Å, $c = 5.1288$ Å and $\alpha = \gamma = 90°$, $\beta = 99.54°$. These values differ from those obtained for our synthesized copper oxide powder (Table 1); however, such discrepancies are not unexpected, as numerous studies report deviations from standardized values. In a recent review encompassing more than three hundred studies on crystalline copper oxide nanoparticles, Md. K. H. Shishir *et al.* highlighted significant variability in the physical parameters of synthesized nanoparticles.[36] This variability notably affects particle size and morphology, preferred growth planes, as well as diffraction peak positions and their relative

Table 1 Structural parameters of synthesized $Cu_{1-x}Zn_xO$ samples

Ratio (x)	a (Å)	b (Å)	c (Å)	β (°)	V (Å^3)
0	4.863 ± 0.011	3.433 ± 0.005	5.136 ± 0.010	99.31 ± 0.03	84.64 ± 0.55
0.05	4.758 ± 0.014	3.438 ± 0.005	5.139 ± 0.011	99.47 ± 0.03	82.93 ± 0.54
0.1	4.702 ± 0.012	3.428 ± 0.005	5.138 ± 0.010	99.44 ± 0.03	81.72 ± 0.53
0.2	4.677 ± 0.013	3.439 ± 0.005	5.138 ± 0.010	99.65 ± 0.03	81.51 ± 0.53
0.3	4.695 ± 0.013	3.438 ± 0.005	5.139 ± 0.011	99.42 ± 0.03	81.87 ± 0.53
0.4	4.687 ± 0.012	3.433 ± 0.005	5.136 ± 0.010	99.50 ± 0.03	81.53 ± 0.53
0.5	4.679 ± 0.013	3.433 ± 0.005	5.138 ± 0.011	99.51 ± 0.03	81.42 ± 0.53

intensities. These differences are strongly dependent on the nature of the precursors and the synthesis route employed: physical (laser ablation, sonication…), chemical (solvothermal, hydrothermal, precipitation…), or biological (using plants or microorganisms). This demonstrates the wide variety of metal oxide nanoparticles that can be produced by varying one or more parameters (precursors, operating conditions, synthesis method, *etc.*). It is this diversity that will ultimately enable the precise identification of the key parameters influencing the physicochemical and morphological properties of the synthesized materials. And from there, the selection of the most effective one suited to the intended applications. It should be noted, however, that this is no easy task, given that the various physicochemical and morphological parameters are affected by the full range of experimental conditions, which are often interrelated. It is therefore clear that only a large number of studies, once compiled, will allow us to unambiguously identify the individual and correlated roles of each parameter and/or operating condition.

3.2 Microstructural analysis

The average crystallite size (D) and the lattice micro-strain (ε) were determined form XRD peak broadening using the Scherrer formula and strain equation:[37,38]

$$D = \frac{k\lambda}{\beta \cos \theta} \quad (4)$$

$$\varepsilon = \frac{\beta}{4 \tan \theta} \quad (5)$$

where $k = 0.9$ is the shape factor, λ is the X-ray wavelength, θ is Bragg angle, and β is the full width at half maximum (FWHM) in radians, obtained directly from Gaussian fitting of the diffraction peaks.

The exact values of 2θ and β for the (002) and (111) reflections were determined by fitting the XRD profiles to a Gaussian function of the form:

$$y = y_0 + \frac{A}{w\sqrt{\pi/2}} e^{-2\frac{(x-x_c)^2}{w^2}} \quad (6)$$

where y_0 is the baseline offset, A is the peak area, x_c is the peak position (corresponding to 2θ), and w is related to the FWHM by:

$$\text{FWHM} = w\sqrt{\ln 4} \quad (7)$$

The fitting was performed with the baseline offset $y_0 = 0$, and the parameters peak position (x_c), area (A), and width (w) were optimized. The resulting FWHM (β) and peak position (2θ) for each reflection are shown in Fig. 2.

The specific surface area (SSA) and the theoretical density (ρ) were further estimated using:[23]

$$\text{SSA} = \frac{6}{D \times \rho} \quad (8)$$

$$\rho = \frac{n \times M}{N \times V} \quad (9)$$

where D is the average crystallite size, M is the molar mass, n is the number of formula units per unit cell, N is Avogadro's number, and V is the unit cell volume.

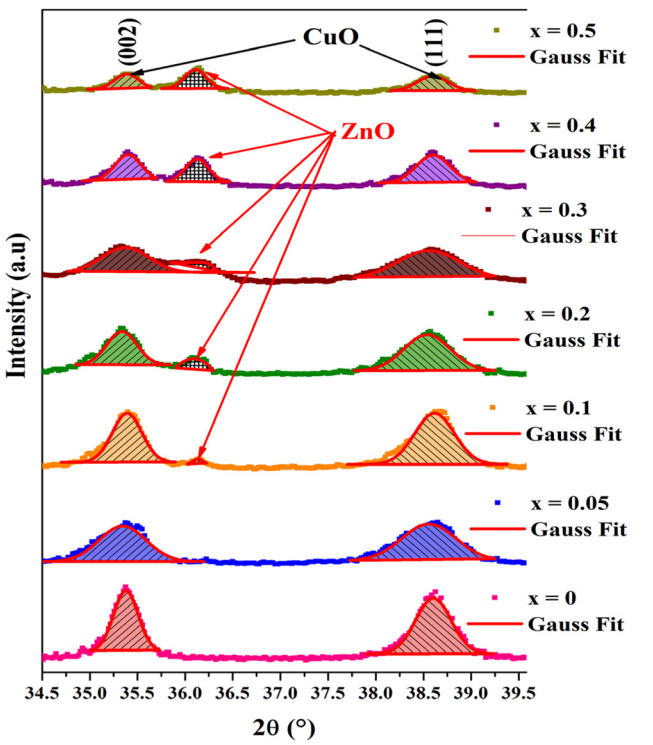

Fig. 2 Gaussian fitting of the (002) and (111) diffraction peaks for a representative $Cu_{1-x}Zn_xO$ ($0 \le x \le 0.5$) samples. The experimental data points are shown as circles, the fitted Gaussian profile as a solid red line, and the residual of the fit is plotted below each profile.

Table 2 Microstructural parameters of $Cu_{1-x}Zn_xO$, determined from the (111) and (002) reflections

Ratio (x)	(hkl)	2θ (°)	β (°)	D (nm)	ε ($\times 10^{-3}$)	ρ (g cm^{-3})	SSA (m^2 g^{-1})
0	(002)	35.380	0.306 ± 0.009	27.23 ± 0.76	4.19 ± 0.12	6.242 ± 0.005	42.37 ± 0.77
	(111)	38.608	0.464 ± 0.008	18.15 ± 0.33	5.78 ± 0.10		
0.05	(002)	35.344	0.577 ± 0.021	14.44 ± 0.51	7.91 ± 0.28	6.371 ± 0.005	70.71 ± 1.60
	(111)	38.556	0.689 ± 0.018	12.21 ± 0.31	8.60 ± 0.22		
0.1	(002)	35.392	0.365 ± 0.013	22.84 ± 0.80	4.99 ± 0.18	6.466 ± 0.005	46.57 ± 1.11
	(111)	38.616	0.495 ± 0.014	17.01 ± 0.50	6.16 ± 0.18		
0.2	(002)	35.387	0.705 ± 0.026	11.83 ± 0.44	9.64 ± 0.36	6.483 ± 0.005	82.67 ± 1.84
	(111)	38.552	0.798 ± 0.018	10.55 ± 0.23	9.96 ± 0.22		
0.3	(002)	35.332	0.440 ± 0.019	18.95 ± 0.81	6.03 ± 0.26	6.454 ± 0.005	56.39 ± 1.50
	(111)	38.538	0.599 ± 0.015	14.04 ± 0.35	7.48 ± 0.18		
0.4	(002)	35.404	0.299 ± 0.013	27.85 ± 1.18	4.09 ± 0.17	6.481 ± 0.005	40.00 ± 1.16
	(111)	38.599	0.456 ± 0.016	18.44 ± 0.64	5.69 ± 0.20		
0.5	(002)	35.389	0.305 ± 0.013	27.34 ± 1.20	4.17 ± 0.18	6.490 ± 0.005	39.14 ± 1.12
	(111)	38.594	0.422 ± 0.013	19.93 ± 0.62	5.26 ± 0.16		

The calculated microstructural parameters for the (002) and (111) reflections of CuO are compiled in Table 2.

The microstructural analysis presented in Table 2 reveals a clear dependence of crystallite size, lattice strain, and specific surface area (SSA) on the Zn doping level (x) in the $Cu_{1-x}Zn_xO$ system. These parameters are fundamental descriptors of the material's nanostructure and are critically linked to its interfacial interactions with bacterial cells.[39] A high SSA, as seen for $x = 0.2$ (82.67 m^2 g^{-1}), provides a greater density of exposed surface sites. This directly enhances the potential for nanoparticle adhesion to cell walls, ion-release kinetics (Cu^{2+}/Zn^{2+}), and the generation of reactive oxygen species (ROS), all key mechanisms in anti-biofilm activity.[40] Concurrently, the minimized crystallite size and maximized lattice strain at this composition indicate high surface energy and defect density, which are known to augment the antimicrobial potency of metal oxides.[35]

The average crystallite size ($D_{avg.}$) exhibits a pronounced non-monotonic evolution with increasing Zn content. The pure CuO ($x = 0$) exhibits a moderate crystallite size of approximately 22.7 nm. Upon initial Zn doping ($x = 0.05$), a sharp decrease in size to about 13.3 nm is observed. This reduction is attributed to the incorporation of Zn^{2+} ions into the CuO lattice, which introduces significant lattice distortion and strain, thereby inhibiting crystallite growth during synthesis.[35] The crystallite size reaches a minimum of approximately 11.2 nm at a doping level of $x = 0.2$. Concurrently, the lattice micro-strain ($\varepsilon_{avg.}$) peaks at 9.6×10^{-3} for this composition, confirming that the maximum structural distortion coincides with the most refined crystallite morphology. For higher Zn concentrations ($x = 0.4$ and 0.5), the crystallite size increases again to approximately 23 nm. This resurgence may indicate a saturation of Zn in the monoclinic CuO lattice, the onset of secondary phase formation, or a shift in nucleation and growth kinetics that favors larger crystalline domains.[32]

The specific surface area (SSA), calculated from the average crystallite size and theoretical density *via* eqn (8), shows an inverse relationship with the crystallite size trend. Consequently, the SSA is maximized for the sample with the smallest crystallites. The composition $x = 0.2$ possesses the highest SSA of 82.67 m^2 g^{-1}, which is nearly double that of the undoped sample (42.37 m^2 g^{-1}). This substantial enhancement is of paramount importance for anti-biofilm applications. A high SSA directly translates to a greater density of exposed surface atoms and active sites, which can promote stronger interactions with bacterial cell walls, enhance the release of antibacterial ions (Cu^{2+}, Zn^{2+}), and facilitate the generation of reactive oxygen species, key factors in disrupting biofilm formation and viability.[39,41]

In summary, the strategic incorporation of Zn into the CuO matrix serves as an effective microstructural engineering tool. The doping process directly influences the crystallite size and internal strain, which in turn govern the specific surface area, a critical property for surface-mediated antimicrobial processes. The composition $x = 0.2$ is identified as optimal within this series, offering the most favorable combination of nanoscale refinement and maximized surface area. These findings underscore the profound impact of dopant-controlled microstructure on tailoring the physicochemical properties of metal oxides for advanced anti-biofilm applications.[42]

3.3 Morphological, topographical, and elemental characterization

3.3.1 Surface morphology and particle size distribution (SEM). Scanning electron microscopy (SEM) was used to investigate the surface morphology and particle size distribution of the $Cu_{1-x}Zn_xO$ nanopowders. Representative SEM micrographs (Fig. 3) along with corresponding 3D surface reconstructions generated using ImageJ software show that all samples exhibit agglomerated quasi-spherical nanoparticles, with agglomeration likely arising from interparticle interactions (*e.g.*, van der Waals forces) during drying and calcination.[43]

Particle size distributions were determined by analyzing multiple SEM images using ImageJ, and the data were fitted to a log-normal distribution function (eqn (10)):[44,45]

$$f(D) = \left(\frac{1}{\sqrt{2\pi} \times \sigma \times D}\right) \exp\left[-\frac{\ln^2\left(\frac{D}{D_0}\right)}{2\sigma^2}\right] \quad (10)$$

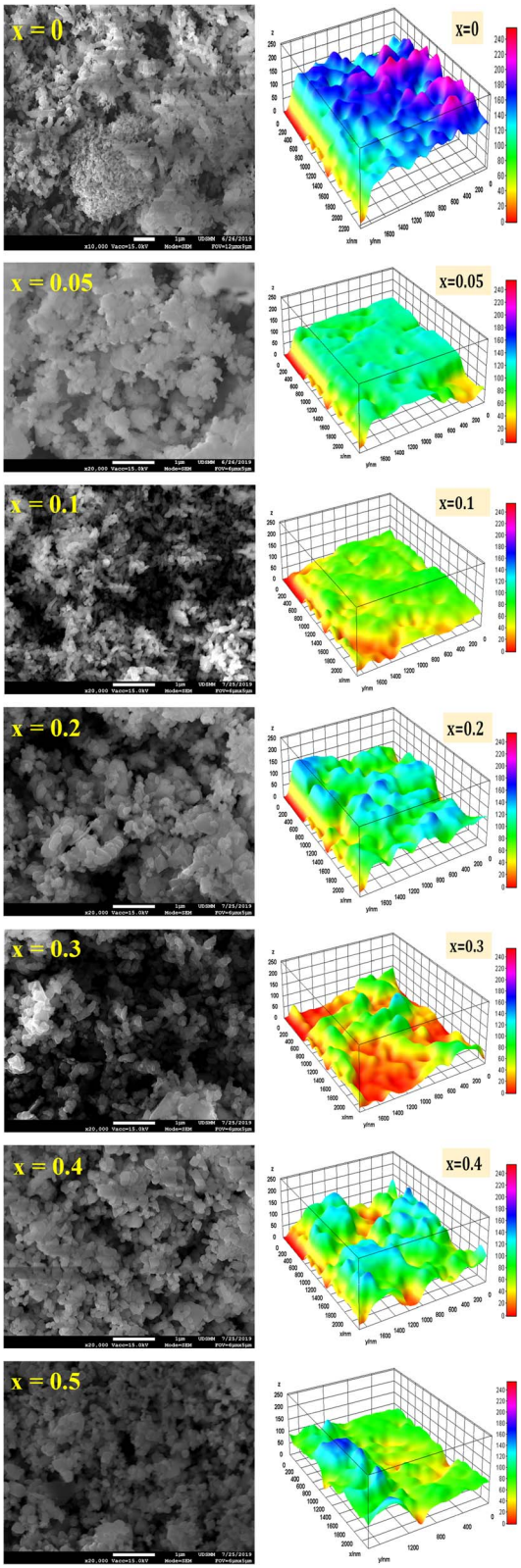

Fig. 3 High-resolution SEM images and 3D-Surface reconstructions of $Cu_{1-x}Zn_xO$ samples obtained from image analysis using ImageJ software.

where $f(D)$ is the log-normal probability density function, D_0 corresponds to the median diameter and σ is the standard deviation of the natural logarithm of the particle diameters.

The resulting histograms and fitted curves are presented in Fig. 4, and the average particle size (D_{SEM}) along with standard deviations (σ) are summarized with error bars representing the standard deviation.

A non-monotonic variation in D_{SEM} with Zn content is observed. At low doping levels ($x \leq 0.1$), D_{SEM} decreases, suggesting that Zn incorporation inhibits CuO grain growth, possibly by segregating at grain boundaries.[32] However, for $x = 0.4$ and 0.5, an increase in D_{SEM} is noted, which may be attributed to excessive Zn promoting particle coalescence or Ostwald ripening due to altered defect chemistry.[40] Intermediate compositions ($x = 0.2$, 0.3) show irregular fluctuations, indicating possible inhomogeneous doping or phase separation effects.[46]

Importantly, the SEM-derived particle sizes are consistently larger than the crystallite sizes obtained from XRD (Table 5), confirming the polycrystalline and aggregated nature of the nanoparticles.[44]

3.3.2 Surface topography and roughness (AFM). Atomic force microscopy (AFM) in tapping phase contrast mode was employed to assess the surface topography and nanoscale roughness of the samples. Fig. 5 displays 2D AFM images (2 × 2 μm scan area), revealing a granular morphology with columnar grain structures. Quantitative roughness parameters, root mean square roughness (S_q), peak roughness (S_p), and valley roughness (S_v), were extracted and are listed in Table 3.

A general reduction in average grain size is observed with increasing Zn content, from approximately 88 nm for pure CuO to 62 nm for $x = 0.5$. This refinement in grain size, coupled with changes in S_q, S_p, and S_v, indicates that Zn doping modifies surface topography, which may influence nanoparticle-bacteria interactions.[47]

3.3.3 Elemental composition and doping confirmation (EDX). Energy-dispersive X-ray spectroscopy (EDX) was performed to verify the elemental composition and confirm successful Zn incorporation. The EDX spectra for all samples (Fig. 6) display characteristic peaks for Cu, Zn, and O. The numerical values presented on the spectra are in atomic percentage (at%). The carbon signal originates from the conductive adhesive used for sample mounting. A weak sulfur peak, attributable to residual sulfate from the $CuSO_4 \cdot 5H_2O$ precursor, is also detected.[48]

The atomic percentages (at%) of Cu, Zn, and O obtained from EDX quantitative analysis are presented in Table 4. The experimental Zn content (x_{EDX}) closely matches the nominal stoichiometry, confirming effective incorporation. For example, the sample with nominal $x = 0.2$ shows an experimental Zn content of 17.7 at%, demonstrating good agreement within instrumental uncertainty.[49] These results validate the successful synthesis of $Cu_{1-x}Zn_xO$ solid solutions and composites as intended.

3.3.4 Comparative analysis of sizing techniques. A comparison of grain sizes obtained from SEM (image analysis), AFM (topography) is summarized in Table 5, which also presents the crystallite size, estimated from XRD measurements.

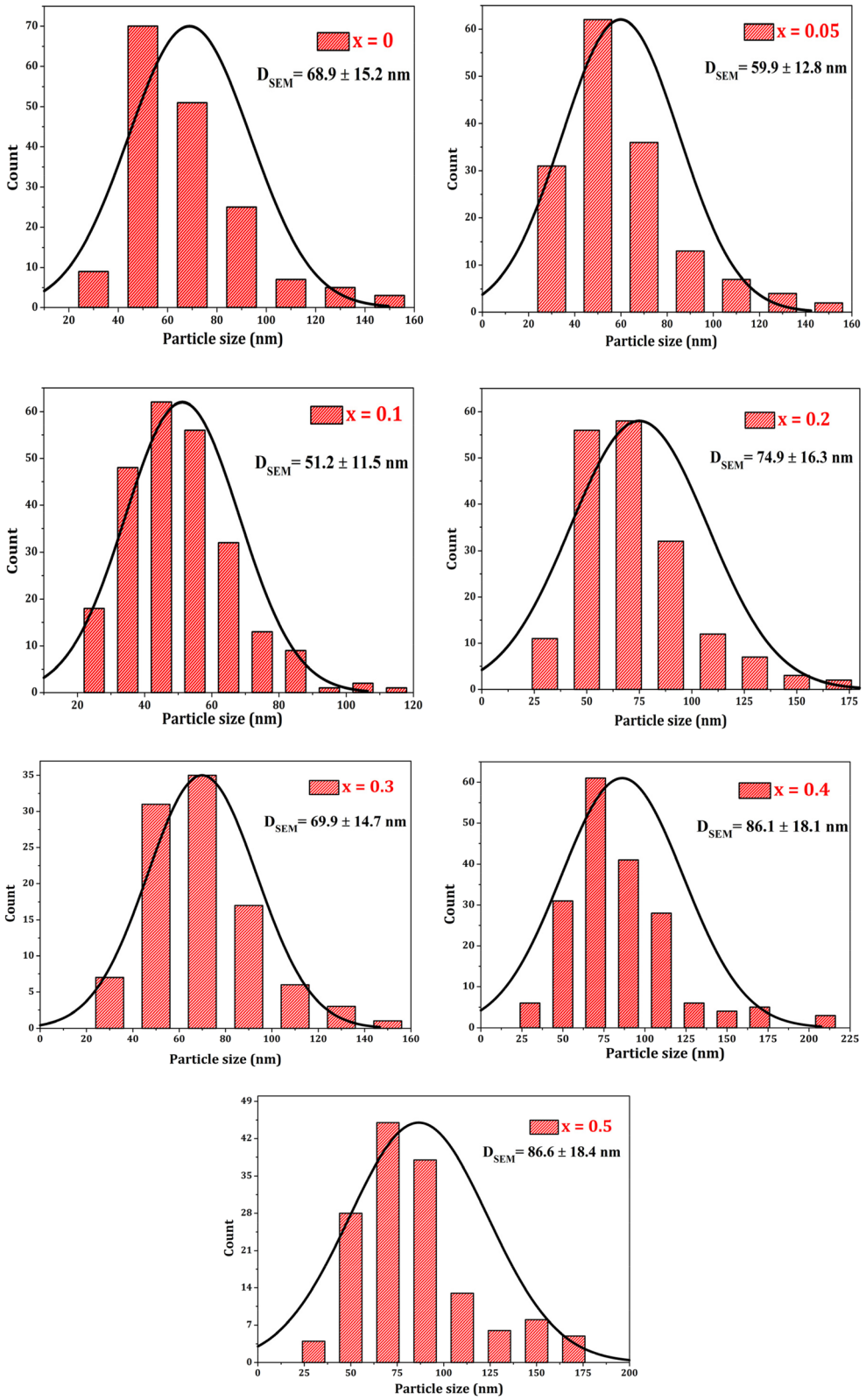

Fig. 4 Average size and particle size distribution (D_{SEM}) with standard deviation (σ) of prepared samples.

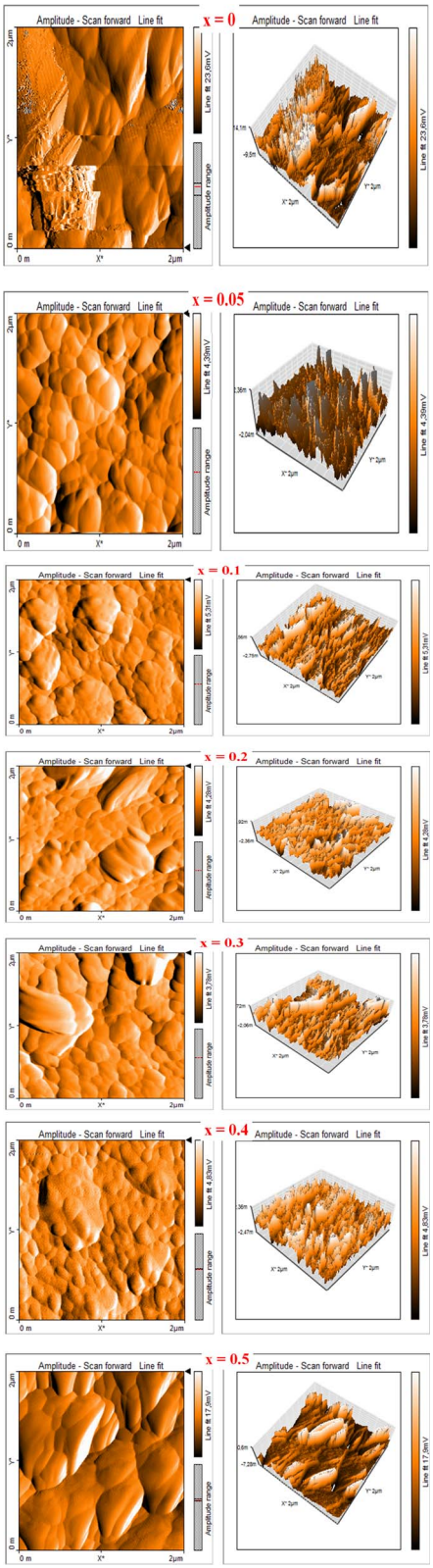

Fig. 5 Two-dimensional (2D) AFM images within the scanning area (2 μm × 2 μm) showing individual columnar grains of the prepared samples.

Table 3 Roughness parameters and average grain size (D_{AFM}) from AFM for $Cu_{1-x}Zn_xO$ in a 2 μm × 2 μm measurement zone

Sample (x)	S_q (nm)	S_p (nm)	S_v (nm)	D_{AFM} (nm)
0	215.1	487.1	−824.4	87.8 ± 5.6
0.05	30.9	96.1	−104.6	74.1 ± 4.9
0.1	28.9	101.9	−82.2	71.4 ± 5.1
0.2	24.8	101.3	−75.5	70.1 ± 4.8
0.3	26.0	106.9	−114.9	68.9 ± 4.5
0.4	33.3	89.3	−103.4	68.0 ± 4.2
0.5	144.3	370.2	−511.6	61.6 ± 4.0

This multi-technique approach provides a comprehensive view of the hierarchical structure: nanocrystalline primary particles (XRD) that aggregate into larger grains (SEM/AFM), a morphology relevant to surface-area-dependent applications such as biofilm inhibition.[50] Both SEM and AFM measurements converge to a mean of four crystallites per nanoparticle.

A comprehensive analysis of these data reveals strong agreement between Atomic Force Microscopy and Scanning Electron Microscopy measurements, both converging to a mean of four crystallites per nanoparticle (4.1 ± 0.4 by AFM and 4.1 ± 1.0 by SEM). When considered individually, these proportions show no correlation with the substitution rate x of copper by zinc, the highest number of crystallites per particle being observed at zinc contents of 5% and 20%. However, considering additional crystallographic parameters reveals a relative correlation with the lattice micro-strain (ε) values (Table 2). This highlights both the richness and, more importantly, the complexity of these comparative analyses, as the key parameters remain difficult to identify due to their cross-correlations.

3.4 Vibrational and surface chemical analysis (FTIR)

Fourier-transform infrared (FTIR) spectroscopy was employed to identify the functional groups, surface chemistry, and chemical bonding in the $Cu_{1-x}Zn_xO$ nanopowders. The spectra, recorded in the range of 400–4000 cm^{-1}, are presented in Fig. 7, with magnified views highlighting three key spectra regions.

The FTIR spectra (Fig. 7) were analyzed in three distinct regions:

Low-frequency region (400–700 cm^{-1}): the strong band below 600 cm^{-1} is attributed to Cu–O stretching vibration in the monoclinic CuO lattice (Fig. 7a).[51,52] With increasing Zn content, this band broadens and shifts slightly, indicating lattice distortion and the possible formation of Zn–O bonds.[53,54] For samples with $x \geq 0.3$, an additional shoulder near 430 cm^{-1} appears, corresponding to Zn–O stretching in the wurtzite ZnO phase,[55] corroborating the XRD evidence of a biphasic composite.

Mid-frequency region (900–1600 cm^{-1}): weak bands between 750–879 cm^{-1} and 987–997 cm^{-1} are associated with vibrational modes of residual sulfate (SO_4^{2-}) groups, originating from the $CuSO_4 \cdot 5H_2O$ precursor (Fig. 7b).[23,56] Their presence confirms that trace sulfate residues persist despite repeated washing, a common feature in wet-chemically synthesized CuO.[57] The absence of organic contaminant peaks (*e.g.*, C–H, C=O)

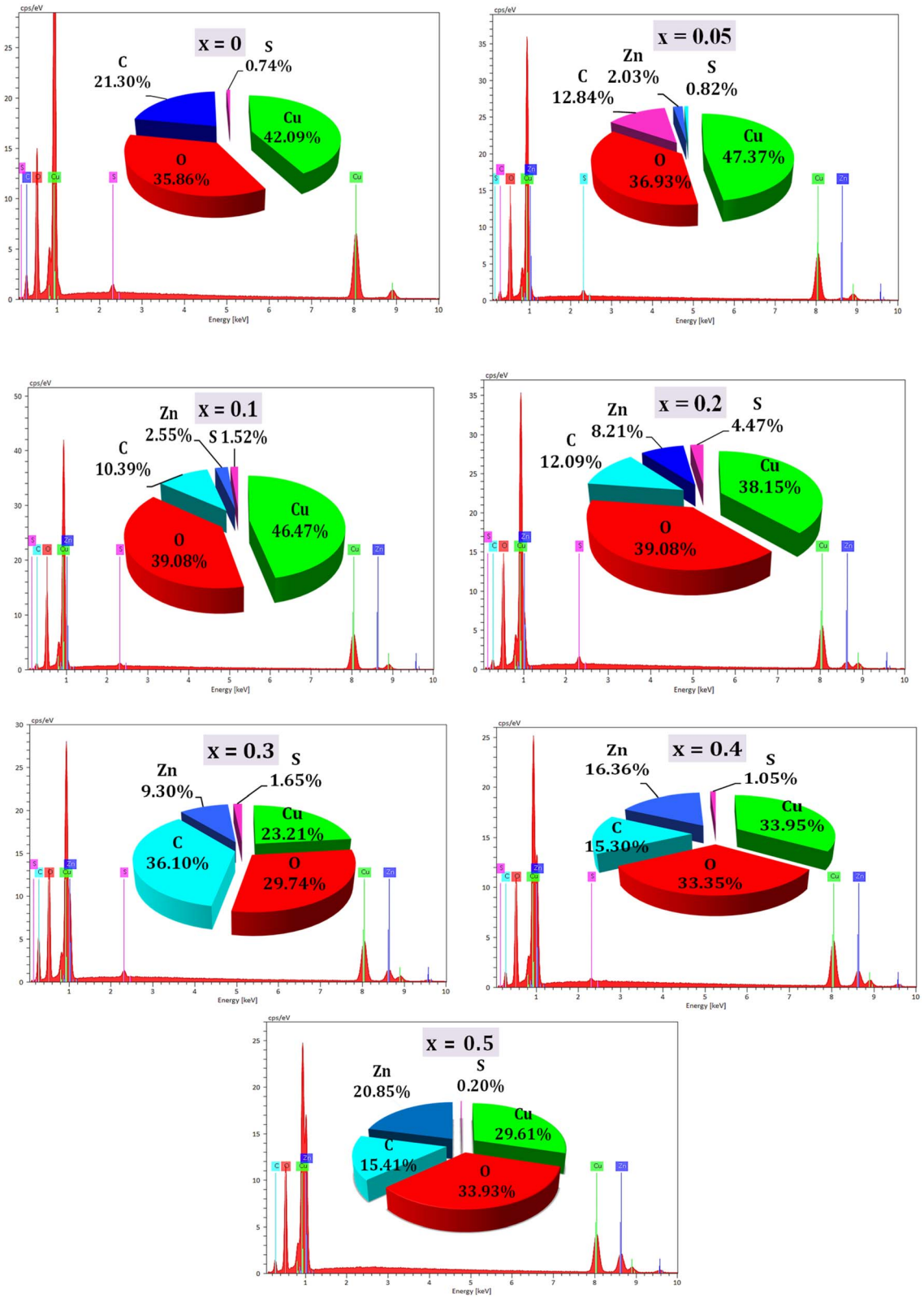

Fig. 6 Elemental determination of synthesized $Cu_{1-x}Zn_xO$ ($0 \leq x \leq 0.5$) powders with elemental compositions reported in atomic percentage (at%).

Table 4 Comparison between nominal and experimental ratio x in $Cu_{1-x}Zn_xO$ particles from EDX analysis in atomic percentage (at%). Uncertainties are between 2% and 8%

Nominal (x)	Cu (at%)	O (at%)	Zn (at%)	Experimental ratio x
0	54.00	46.00	0.00	0
0.05	54.87	42.78	2.35	0.041 ± 0.004
0.1	52.74	44.36	2.90	0.052 ± 0.005
0.2	44.65	45.74	9.61	0.177 ± 0.014
0.3	37.29	47.78	14.94	0.286 ± 0.020
0.4	40.59	39.86	19.55	0.325 ± 0.020
0.5	35.09	40.20	24.71	0.413 ± 0.021

confirms the effectiveness of the calcination step in producing pure oxide phases.[58]

High-frequency region (2700–4000 cm^{-1}): a broad absorption band centered around 3400 cm^{-1} is observed in all samples (Fig. 7c), corresponding to O–H stretching vibrations from surface-adsorbed water molecules and hydroxyl groups.[59,60] This hydrophilic character is typical of metal oxide nanoparticles and may influence their dispersion in aqueous media and interaction with bacterial surfaces.

The FTIR results collectively support the structural evolution deduced from XRD: at low x, Zn integrates into the CuO lattice; at higher x, a biphasic CuO/ZnO composite forms, with surface chemistry progressively influenced by the ZnO phase.

3.5 Anti-adhesive activity against biofilm-forming bacteria

3.5.1 Activity against Gram-positive *S. epidermidis* S61. The anti-adhesive efficacy of $Cu_{1-x}Zn_xO$ nanoparticles against the Gram-positive bacterium *S. epidermidis* S61 was evaluated using a crystal violet biofilm inhibition assay. As shown in Fig. 8, undoped CuO NPs exhibit dose-dependent anti-adhesive activity, ranging from 4.7% inhibition at 7.8 μg mL^{-1} to 53.3% at 500 μg mL^{-1}.

Zn doping significantly modulates this activity. The sample with $x = 0.2$ demonstrates the most potent effect, achieving >72% inhibition at both 250 and 500 μg mL^{-1}. In contrast, the highly doped sample ($x = 0.5$) shows a substantial loss of activity at low concentrations (7.8–62.5 μg mL^{-1}), highlighting a concentration- and composition-dependent response. Interestingly, low to moderate Zn doping ($x = 0.05$ and 0.4) enhances the low-concentration activity compared to pure CuO. For instance, at 7.8 μg mL^{-1}, samples with $x = 0.05$ and 0.4 achieve ~21% inhibition, whereas pure CuO yields only 4.7%. These results suggest that optimized Zn doping enhances the anti-adhesive performance of CuO against Gram-positive bacteria, likely by modifying surface properties and reactive ion release.[18,40]

3.5.2 Activity against Gram-negative *P. aeruginosa* 2629. A distinctly different trend is observed against the Gram-negative bacterium *P. aeruginosa* 2629 (Fig. 9). Here, pure CuO exhibits the strongest anti-adhesive activity, particularly at high concentrations (500 μg mL^{-1}). Zn doping generally reduces efficacy against this strain. Most doped samples show significant activity only at the highest concentration tested (500 μg mL^{-1}), while pure CuO maintains notable inhibition across a broader concentration range (3.9–62.5 μg mL^{-1}).

This clear divergence in response underscores a strain- and cell-wall-dependent mechanism. The superior performance of pure CuO against *P. aeruginosa* may be linked to its interaction with the outer membrane lipopolysaccharides (LPS) of Gram-negative bacteria, which is potentially disrupted by Zn doping.[25,61]

3.5.3 Comparative efficacy and bacterial selectivity. A direct comparison of the maximum anti-adhesive activity (at 500 μg mL^{-1}) against both bacterial strains is presented in Fig. 10. This visualization highlights the selectivity of the nanomaterials:

- For *S. epidermidis* (GP), optimal activity is achieved with $x = 0.2$.
- For *P. aeruginosa* (GN), pure CuO ($x = 0$) is most effective.
- The sample with $x = 0.5$ shows moderate activity against both strains but is less efficient than the optimized compositions for each specific bacterium.

This selectivity is crucial for designing targeted anti-biofilm strategies and can be rationalized by fundamental differences in bacterial cell wall structure (Fig. 11). Gram-positive bacteria possess a thick peptidoglycan layer, while Gram-negative bacteria feature an additional outer membrane containing LPS. These structural differences influence nanoparticle attachment, ion permeability, and subsequent bactericidal effects.[25,26] Furthermore, variations in surface charge and extracellular polymeric substance (EPS) composition between GP and GN biofilms contribute to the observed differential activity.[62,63]

The anti-adhesive mechanism likely involves a combination of direct nanoparticle interaction with bacterial cell walls, release of antibacterial Cu^{2+} and Zn^{2+} ions, and the generation of reactive oxygen species (ROS), as schematically illustrated in Fig. 12.[38,64,65] The composition-dependent modulation of these

Table 5 Comparative microstructural analysis of $Cu_{1-x}Zn_xO$ samples from different techniques

Ratio (x)	Crystallites $D_{avg.}$ (nm)	Particles D_{SEM} (nm)	Particles D_{AFM} (nm)	Crystallite/particle ratio	
				SEM	AFM
0	22.69 ± 0.41	68.9 ± 15.2	87.8 ± 5.6	3.0 ± 0.7	3.9 ± 0.3
0.05	13.33 ± 0.30	59.9 ± 12.8	74.1 ± 4.9	4.5 ± 1.1	5.6 ± 0.5
0.1	19.92 ± 0.47	51.2 ± 11.5	71.4 ± 5.1	2.6 ± 0.6	3.6 ± 0.3
0.2	11.19 ± 0.25	74.9 ± 16.3	70.1 ± 4.8	6.7 ± 1.6	6.3 ± 0.6
0.3	16.49 ± 0.44	69.9 ± 14.7	68.9 ± 4.5	4.2 ± 1.0	4.2 ± 0.4
0.4	23.14 ± 0.67	86.1 ± 18.1	68.0 ± 4.2	3.7 ± 0.9	2.9 ± 0.3
0.5	23.63 ± 0.68	86.6 ± 18.4	61.6 ± 4.0	3.7 ± 0.9	2.6 ± 0.2

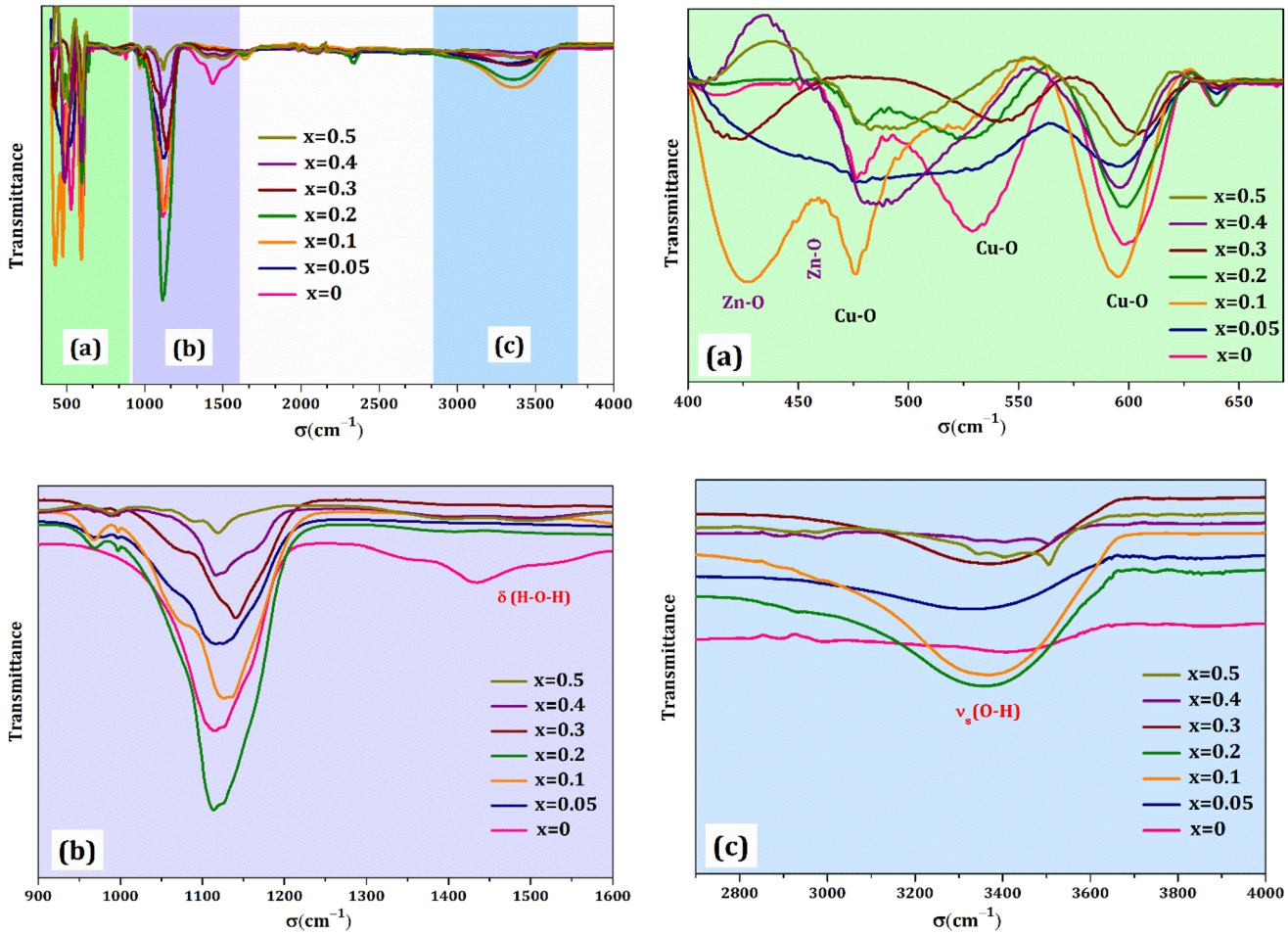

Fig. 7 FTIR spectra of $Cu_{1-x}Zn_xO$ samples in full range (400–4000 cm^{-1}); (a) low-frequency region (400–700 cm^{-1}), (b) mid-frequency region (900–1600 cm^{-1}), (c) high-frequency region (2700–4000 cm^{-1}).

factors by Zn doping explains the strain-specific efficacy profiles observed in this study.

3.6 Synthesis of structure–property–activity relationships and mechanisms

3.6.1 Correlation between structural properties and Zn doping. This study demonstrates that Zn doping significantly alters the structural, morphological, and surface properties of CuO nanoparticles. XRD and FTIR analyses confirm that for $x \leq 0.05$, Zn^{2+} ions substitute Cu^{2+} in the monoclinic lattice, while for $x \geq 0.1$, a biphasic CuO/ZnO nanocomposite forms. This phase evolution directly impacts physical parameters such as crystallite size, lattice strain, and specific surface area (SSA). The reduction in SSA at certain doping levels (*e.g.*, $x = 0.4$, 0.5) may be attributed to increased crystallite size or denser aggregation, whereas samples with higher SSA (*e.g.*, $x = 0.05$, 0.2) possess more exposed surface sites potentially active against bacteria.[39,41]

Morphological analysis *via* SEM and AFM reveals that Zn doping generally reduces grain size and modifies surface roughness, factors known to influence nanomaterial–cell interactions.[66] EDX quantification confirms that the synthesized compositions closely match the intended stoichiometries, validating the co-precipitation method as a reliable route for producing doped and composite oxide nanoparticles.

3.6.2 Strain-specific anti-biofilm activity: role of bacterial cell-wall architecture. The most striking finding of this work is the strain-dependent anti-adhesive response to Zn doping. Against the Gram-positive *S. epidermidis*, optimal Zn doping ($x = 0.2$) enhances anti-adhesive activity, particularly at higher concentrations. In contrast, against the Gram-negative *P. aeruginosa*, pure CuO outperforms all doped samples.

This divergence can be rationalized by fundamental differences in cell envelope structure (Fig. 11). This thick, porous peptidoglycan layer of Gram-positive bacteria may facilitate deeper penetration and interaction with smaller, doped nanoparticles, where Zn-induced surface defects enhance reactive oxygen species (ROS) generation or ion release.[25,40] Conversely, the outer membrane of Gram-negative bacteria, rich in lipopolysaccharides (LPS), presents a formidable permeability barrier.[26] Pure CuO, with its distinct surface chemistry and

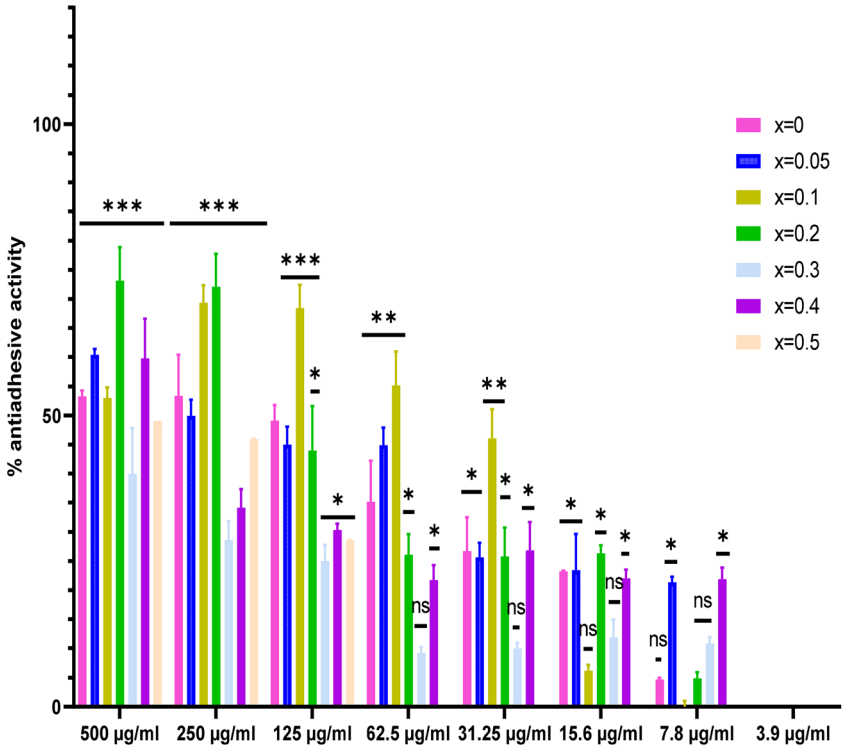

Fig. 8 Anti-adhesive activities of $Cu_{1-x}Zn_xO$ nanopowders applied at different concentrations against *S. epidermidis* S61. Experiments were performed in triplicate; results were presented as mean ± SD from three independent experiments (significance levels compared to untreated control are denoted as $*p < 0.05$; $**p < 0.01$; $***p < 0.001$).

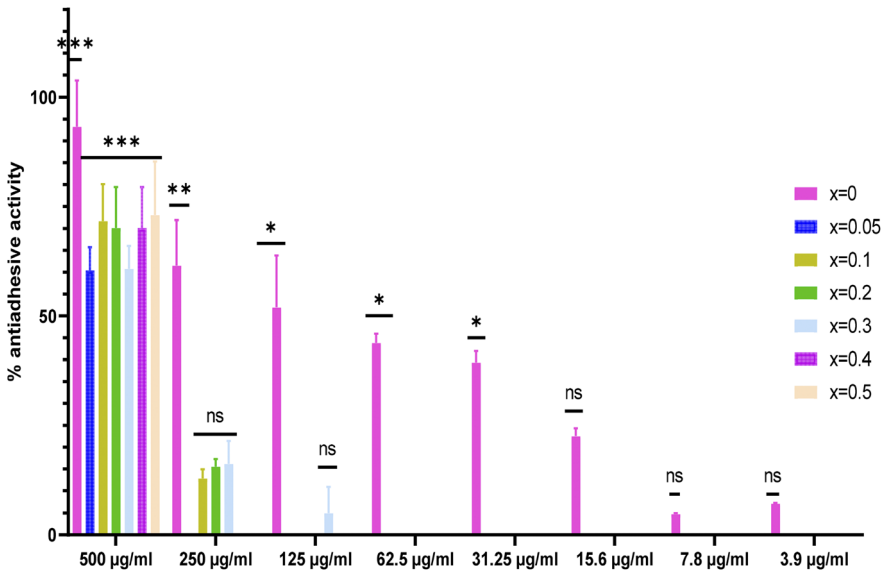

Fig. 9 The anti-adhesive activities of $Cu_{1-x}Zn_xO$ nanopowders investigated at various concentrations against *P. aeruginosa* 2629. Experiments were performed in triplicate; results were presented as mean ± SD from three independent experiments (significance levels compared to untreated control are denoted as $*p < 0.05$; $**p < 0.01$; $***p < 0.001$).

dissolution profile, may interact more effectively with LPS, disrupting membrane integrity and inhibiting adhesion.[61,63]

3.6.3 Proposed mechanism of anti-adhesive action. The anti-adhesive activity of $Cu_{1-x}Zn_xO$ nanoparticles likely involves a multimodal mechanism (Fig. 12):

1. *Physical disruption*: nanoparticles adsorb onto the bacterial surface or biofilm matrix, interfering with initial attachment and biofilm stability.[67]

2. *Ion release*: Cu^{2+} and Zn^{2+} ions released from the nanoparticles disrupt *trans*-membrane potentials, enzyme activity, and DNA integrity.[64]

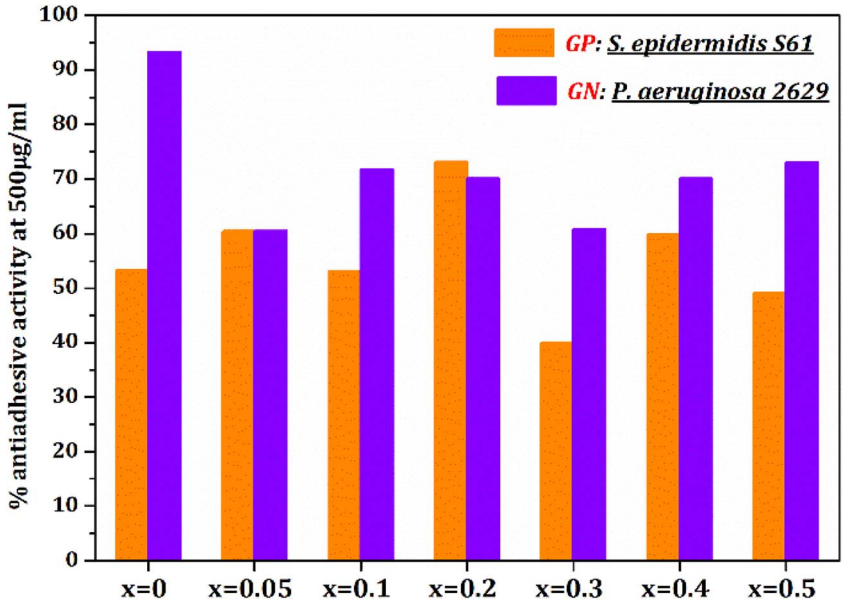

Fig. 10 Comparison of the maximum anti-adhesive activity (%) of samples against *S. epidermidis* S61 and *P. aeruginosa* 2629 at a high concentration of 500 µg mL^{-1}.

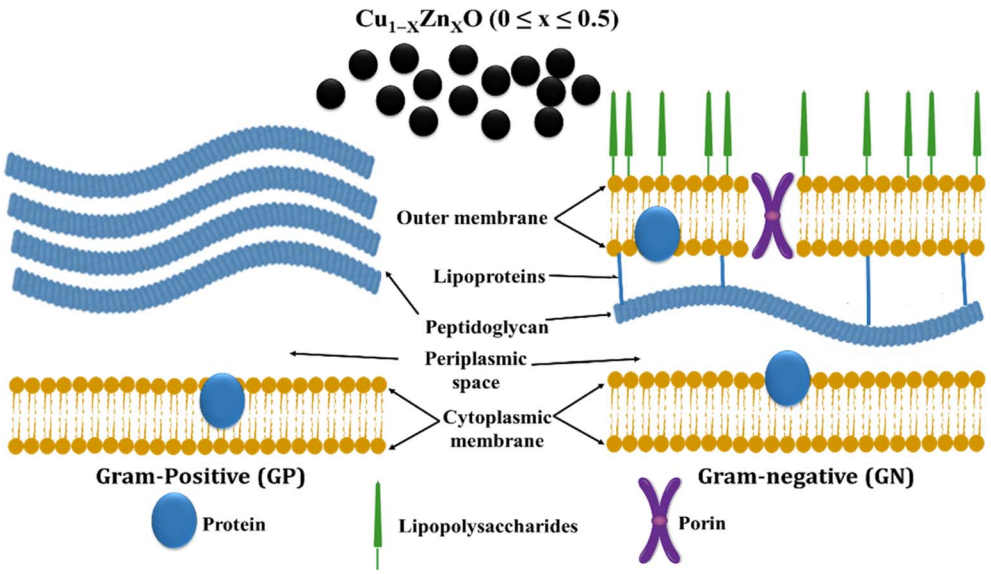

Fig. 11 Schematic of the differences in cell-wall structure of Gram-negative (GN) and Gram-positive (GP) bacteria.

3. *ROS generation*: surface defects and electronic transitions in the metal oxides promote the formation of reactive oxygen species, inducing oxidative stress and damaging cellular components.[65,68]

Zn doping modulates these mechanisms by altering the nanoparticles' electronic structure, dissolution kinetics, and surface reactivity. The optimal doping level differs between bacterial strains, highlighting the importance of tailoring nanomaterial composition for targeted applications.

3.6.4 Implications for biomedical and environmental applications. The tunable and strain-specific anti-biofilm activity of $Cu_{1-x}Zn_xO$ nanoparticles positions them as promising candidates for several practical applications. In the biomedical field, they could be integrated into antimicrobial coatings for medical devices, implants, and hospital surfaces to prevent biofilm-associated infections, following similar strategies employed with other metal oxide nanomaterials.[67,69] Similarly, their incorporation into functional textiles for healthcare environments could reduce microbial colonization and transmission, as demonstrated in recent studies on nanoparticle-functionalized fabrics.[23] Beyond biomedical uses, these nanomaterials also hold potential for environmental remediation, serving as biofilm-inhibiting agents in water treatment systems or in industrial settings prone to biofouling, an area where CuO

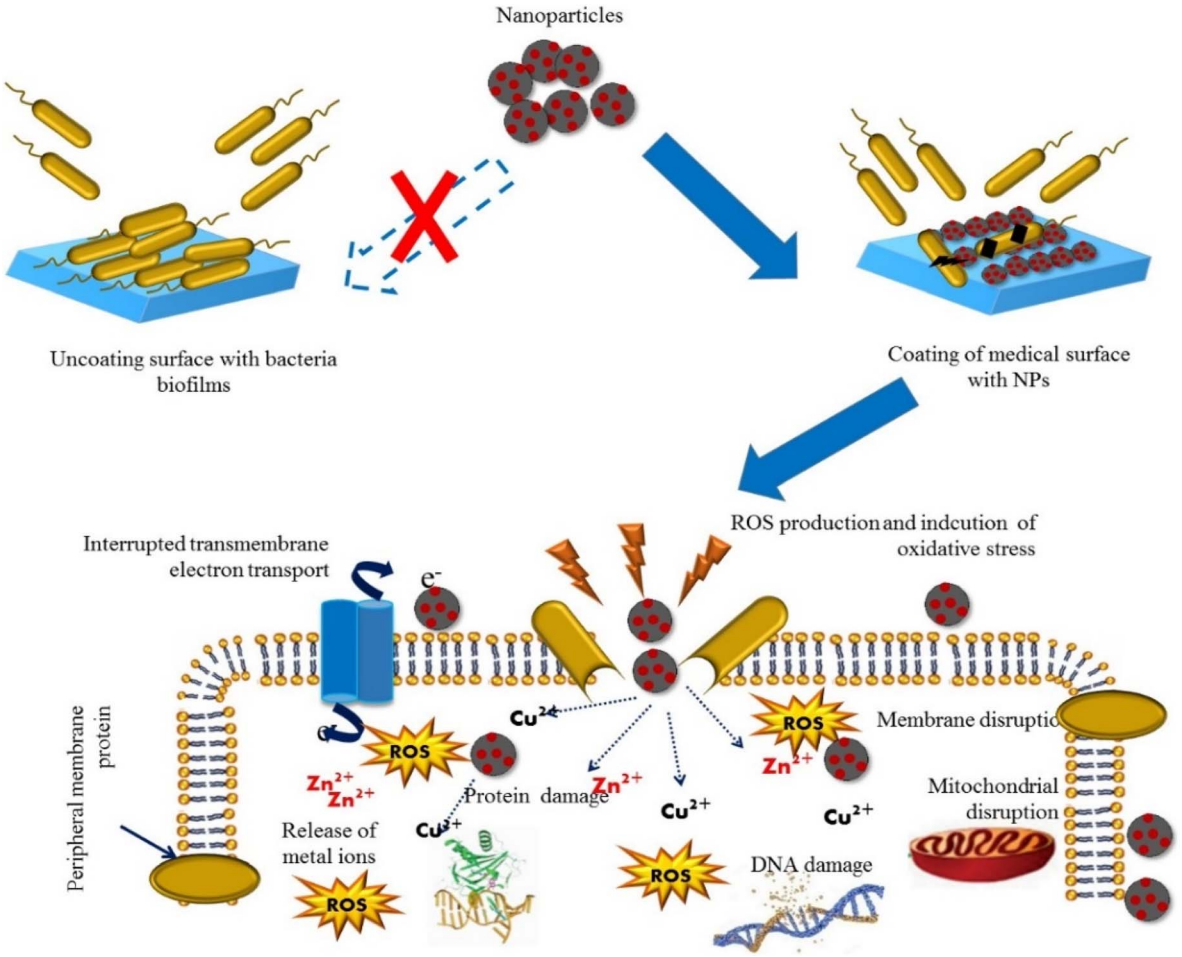

Fig. 12 Schema describing the anti-adhesive activity and the mechanisms of interaction between the nanoparticles and bacterial cells.

and ZnO composites have shown preliminary promise.[70] Future research should focus on evaluating their *in vivo* efficacy, long-term stability, biocompatibility, and cytotoxicity, as well as elucidating the detailed molecular mechanisms underlying their strain-specific anti-adhesive action, including gene expression studies of biofilm-related genes. Exploring synergistic effects with conventional antibiotics in another promising avenue.

4 Conclusion & future perspective

In summary, a series of $Cu_{1-x}Zn_xO$ ($0 \leq x \leq 0.5$) nanoparticles was successfully synthesized *via* co-precipitation and systematically characterized. XRD and FTIR revealed a transition from Zn-substituted CuO solid solutions ($x \leq 0.05$) to CuO/ZnO nanocomposites ($x \geq 0.1$). Morphological analysis showed that Zn doping influences grain size, aggregation, and surface roughness. The anti-adhesive activity against biofilm-forming bacteria is strongly dependent on both nanoparticle composition and bacterial strain. Optimal Zn doping ($x = 0.2$) maximizes activity against Gram-positive *S. epidermidis*, whereas pure CuO is most effective against Gram-negative *P. aeruginosa*. This selectivity is attributed to differences in cell-well structure, surface charge, and nanoparticle dissolution behavior.

Despite the promising results, this study has certain limitations. The experiments were conducted exclusively *in vitro* using two bacterial strains, and the potential cytotoxicity of the nanoparticles towards mammalian cells was not assessed. Additionally, the detailed molecular mechanisms underlying the observed strain-specific activity, such as the expression of genes involved in biofilm formation and oxidative stress response, remain to be elucidated.

Future research should address these limitations by extending the investigation to *in vivo* models, evaluating the biocompatibility and log-term stability of the nanoparticles, and performing transcriptomic or proteomic analysis to unravel the molecular pathways involved. Furthermore, the synergistic effects of combining these nanoparticles with conventional antibiotics should be explored as a strategy to combat multidrug-resistant biofilms. The development of nanoparticle-infused coatings for medical devices and implants represents a promising translational pathway for these materials.

By correlating structural characteristics with biological performance, this work advances the development of effective, strain-specific antimicrobial agents for combating biofilm-associated infections in biomedical and industrial contexts. The capacity to tune CuO or composite metallic oxide nanoparticles' properties, through variation of synthesis methods,

can be advantageously exploited to tailor synthesis strategies to targeted applications.

Author contributions

N. Khlifi: writing – original draft, software, formal analysis, conceptualization. S. Mnif: writing – review & editing, supervision, methodology, resources, investigation. C. Zerrouki: writing – review & editing, supervision, methodology, investigation. H. Guermazi: visualization, supervision, methodology. N. Fourati: visualization, supervision, methodology. Benoît Duponchel: resources. S. Aifa: supervision, resources. S. Guermazi: visualization, supervision, resources, project administration.

Conflicts of interest

The authors declare that they have no known competing financial interests or personal relationships that could have appeared to influence the work reported in this manuscript.

Data availability

Data will be made available on request.

Acknowledgements

This research did not receive any specific grant from funding agencies in the public, commercial, or not-for-profit sectors. The authors gratefully acknowledge the support of the Tunisian Ministry of High Education and Scientific Research.

References

1 A. Jain, P. K. Javaregowda, S. S. Kulkarni, R. D. Kulkarni and A. K. Oli, *Rom. J. Infect. Dis.*, 2022, **25**, 97–107.
2 R. Lordelo, R. Branco, F. Gama and P. V. Morais, *Heliyon*, 2024, **10**, e30464.
3 R. Ramakrishnan, A. K. Singh, S. Singh, D. Chakravortty and D. Das, *J. Biol. Chem.*, 2022, **298**, 102352.
4 R. M. Hassan, M. S. Abd El-Maksoud, I. A. Y. Ghannam, A. A.-S. El-Azzouny and M. N. Aboul-Enein, *Eur. J. Med. Chem.*, 2023, **262**, 115867.
5 S. Nadar, T. Khan, S. G. Patching and A. Omri, *Microorganisms*, 2022, **10**, 303.
6 W. Oliveira, P. Silva, R. Silva, G. Silva, G. Machado, L. Coelho and M. Correia, *J. Hosp. Infect.*, 2018, **98**, 111–117.
7 M. del Mar Cendra and E. Torrents, *Biotechnol. Adv.*, 2021, **49**, 107734.
8 S. d. C. Brito, J. O. D. Malafatti, F. E. Arab, J. D. Bresolin, E. C. Paris, C. W. O. de Souza and M. D. Ferreira, *Inorg. Nano-Met. Chem.*, 2023, **53**, 490–500.
9 T. T. T. Nguyen, Y. N. N. Nguyen, X. T. Tran, T. T. T. Nguyen and T. Van Tran, *J. Environ. Chem. Eng.*, 2023, **11**, 111003.
10 W. A. Alwesabi, P. D. Dange, A. V. Raut, G. M. Puri, R. M. Khobragade, P. P. Pawar, S. Pammi, C. K. Kumar and P. Kollu, *J. Supercond. Novel Magn.*, 2024, **37**, 1923–1937.
11 D. P. Mohanan, V. V. Thazhenandayipurath, K. Sreekanth, J. V. Stanley, D. Mathew, N. Radhakrishnan and R. E. Krishnankutty, *J. Cluster Sci.*, 2024, **35**, 3065–3079.
12 K. Mamatha, H. Suresh Kumar, T. Puttaraju, T. Soundarya and G. Nagaraju, *Ionics*, 2024, **30**, 7665–7684.
13 Z. Pezeshki-Nejad, S. Alikhanzadeh-Arani and M. A. Kashi, *J. Magn. Magn. Mater.*, 2019, **482**, 301–311.
14 Y. Lv, L. Li, P. Yin and T. Lei, *Dalton Trans.*, 2020, **49**, 4699–4709.
15 A. Khalid, P. Ahmad, A. I. Alharthi, S. Muhammad, M. U. Khandaker, M. Rehman, M. R. I. Faruque, I. U. Din, M. A. Alotaibi and K. Alzimami, *Nanomaterials*, 2021, **11**, 451.
16 N. Corda, R. Thundiyil, A. Ani, P. P. Anusha, A. Rao and K. Manjunatha, *Mater. Res. Express*, 2024, **11**, 056203.
17 N. Thakur, K. Kumar and A. Kumar, *Dalton Trans.*, 2021, **50**, 6188–6203.
18 C. Uthra, K. Nagaraj, M. A. Wadaan, C. Karuppiah, P. Maity, A. Baabbad, R. Kaliyaperumal, R. Venkatachalapathy, F. Shah and P. Kumar, *Materials*, 2024, **17**, 3444.
19 A. Peter, M. D. Ramesh, E. Bindiya and S. G. Bhat, *Results Eng.*, 2023, **17**, 100998.
20 A. N. Generalova and A. O. Dushina, *Adv. Colloid Interface Sci.*, 2025, 103626.
21 N. A. Jasim, F. A. Al-Gasha'a, M. F. Al-Marjani, A. H. Al-Rahal, H. A. Abid, N. A. Al-Kadhmi, M. Jakaria and A. M. Rheima, *Biocatal. Agric. Biotechnol.*, 2020, **29**, 101745.
22 A. Awasthi, P. Sharma, L. Jangir, G. Awasthi, K. K. Awasthi and K. Awasthi, *Mater. Sci. Eng. C*, 2020, **113**, 111021.
23 N. Khlifi, S. Mnif, F. B. Nasr, N. Fourati, C. Zerrouki, M. Chehimi, H. Guermazi, S. Aifa and S. Guermazi, *RSC Adv.*, 2022, **12**, 23527–23543.
24 M. Maruthapandi, A. Saravanan, P. Das, M. Natan, G. Jacobi, E. Banin, J. H. Luong and A. Gedanken, *ACS Appl. Polym. Mater.*, 2020, **2**, 5878–5888.
25 N. Tripathi and M. K. Goshisht, *ACS Appl. Bio Mater.*, 2022, **5**, 1391–1463.
26 T. D. Tavares, J. C. Antunes, J. Padrão, A. I. Ribeiro, A. Zille, M. T. P. Amorim, F. Ferreira and H. P. Felgueiras, *Antibiotics*, 2020, **9**, 314.
27 M. Jardak, F. Abdelli, R. Laadhar, R. Lami, D. Stien, S. Aifa and S. Mnif, *J. Gen. Appl. Microbiol.*, 2017, **63**, 186–194.
28 A. Nostro, A. S. Roccaro, G. Bisignano, A. Marino, M. A. Cannatelli, F. C. Pizzimenti, P. L. Cioni, F. Procopio and A. R. Blanco, *J. Med. Microbiol.*, 2007, **56**, 519–523.
29 S. F. Mohammed, R. A. Lateef and O. A. Mahmood, *Nahrain J. Sci.*, 2025, **28**, 144–149.
30 O. B. Messaoud, A. Ouahab, S. Rahmane, S. Hettal, A. Kater, M. Sayad, H. Attouche and N. Gherraf, *Periodica Polytech., Chem. Eng.*, 2024, **68**, 93–105.
31 A. Prakash and M. Mahesha, *Mater. Chem. Phys.*, 2023, **309**, 128443.
32 R. Sirirak, P. Chaopanich, A. Prasatkhetragarn, C. Chailuecha, S. Kuimalee and A. Klinbumrung, *Radiat. Phys. Chem.*, 2022, **190**, 109788.
33 M. B. Mobarak, M. S. Hossain, F. Chowdhury and S. Ahmed, *Arab. J. Chem.*, 2022, **15**, 104117.
34 S. Kamble and V. Mote, *Solid State Sci.*, 2019, **95**, 105936.

35 R. Yathisha, Y. A. Nayaka, P. Manjunatha, H. Purushothama, M. Vinay and K. Basavarajappa, *Phys. E*, 2019, **108**, 257–268.
36 M. K. H. Shishir, M. Islam, N. R. Sayeem, N. S. Anam, M. R. I. Shipon, M. Rifat, S. Ahmed, M. Tauhiduzzaman and M. A. Alam, *Chem. Inorg. Mater.*, 2025, 100123.
37 J. I. Langford and A. Wilson, *J. Appl. Crystallogr.*, 1978, **11**, 102–113.
38 K. Ali, B. Ahmed, S. M. Ansari, Q. Saquib, A. A. Al-Khedhairy, S. Dwivedi, M. Alshaeri, M. S. Khan and J. Musarrat, *Mater. Sci. Eng. C*, 2019, **100**, 747–758.
39 V. Stanić and S. B. Tanasković, in *Nanotoxicity*, Elsevier, 2020, pp. 241–274.
40 P. Kumar, G. K. Inwati, M. C. Mathpal, S. Ghosh, W. Roos and H. Swart, *Appl. Surf. Sci.*, 2021, **560**, 150026.
41 N. Matijaković Mlinarić, S. Altenried, A. Selmani, J. Nikolic, A. Ucakar, A. Zore, A. Abram, S. Lehner, A. S. Skapin and M. Kuster, *ACS Appl. Nano Mater.*, 2024, **7**, 12550–12563.
42 N. Karimi, M. Zarrabeitia, A. Mariani, D. Gatti, A. Varzi and S. Passerini, *Adv. Energy Mater.*, 2021, **11**, 2003521.
43 R. Borah, K. R. Ag, A. C. Minja and S. W. Verbruggen, *Small Methods*, 2023, **7**, 2201536.
44 H. Jalili, B. Aslibeiki, A. G. Varzaneh and V. A. Chernenko, *Beilstein J. Nanotechnol.*, 2019, **10**, 1348–1359.
45 S. K. Paswan, S. Kumari, M. Kar, A. Singh, H. Pathak, J. Borah and L. Kumar, *J. Phys. Chem. Solids*, 2021, **151**, 109928.
46 K. Yang, R. Deng, C. Wang, S. Wu, Z. Cui, Y. Zheng, Z. Li, H. Jiang, S. Zhu and P. K. Chu, *Surf. Interfaces*, 2024, **53**, 105023.
47 K. Neuhaus, P. Mowe and M. Winter, *RSC Appl. Interfaces*, 2025, **2**, 620–633.
48 N. C. Horti, M. D. Kamatagi, N. R. Patil, M. S. Sannaikar and S. R. Inamdar, *J. Nanophotonics*, 2020, **14**, 046010.
49 N. Widiarti, J. Sae and S. Wahyuni, *IOP Conf. Ser.:Mater. Sci. Eng.*, 2017, **172**, 012036.
50 A. Ali, S. R. Ali, R. Hussain, R. Anjum, Q. Liu, M. S. Elshikh, N. Alkubaisi, R. Iqbal, S. Tabor and M. Gancarz, *Sci. Rep.*, 2025, **15**, 5010.
51 K. Malook, H. Khan and M. Ali, *Mater. Sci. Semicond. Process.*, 2020, **113**, 105021.
52 N. A. Neto, P. Oliveira, R. Nascimento, C. Paskocimas, M. Bomio and F. Motta, *Ceram. Int.*, 2019, **45**, 651–658.
53 P. Kumar, M. C. Mathpal, J. Prakash, B. C. Viljoen, W. Roos and H. Swart, *J. Alloys Compd.*, 2020, **832**, 154968.
54 A. ur Rehman, M. Aadil, S. Zulfiqar, P. O. Agboola, I. Shakir, M. F. A. Aboud, S. Haider and M. F. Warsi, *Ceram. Int.*, 2021, **47**, 5929–5937.
55 A. Naseri, M. Samadi, N. M. Mahmoodi, A. Pourjavadi, H. Mehdipour and A. Z. Moshfegh, *J. Phys. Chem. C*, 2017, **121**, 3327–3338.
56 N. A. Bakr, T. A. Al-Dhahir and S. B. Mohammad, *J. Adv. Phys.*, 2017, **13**, 4651–4656.
57 G. Wang, Y. Zhang, L. Ge, Z. Liu, X. Zhu, S. Yang, P. Jin, X. Zeng and X. Zhang, *J. Hazard Mater.*, 2022, **429**, 128282.
58 L. Taguelmimt, O. Hamouma, D. Oukil, A. Djermoune, K. Kouachi, R. Aitout, L. Makhloufi and A. Azizi, *J. Water Proc. Eng.*, 2025, **78**, 108810.
59 J. Iqbal, T. Jan, S. Ul-Hassan, I. Ahmed, Q. Mansoor, M. Umair Ali, F. Abbas and M. Ismail, *AIP Adv.*, 2015, **5**, 127209.
60 J. Jayaprakash, N. Srinivasan, P. Chandrasekaran and E. Girija, *Spectrochim. Acta, Part A*, 2015, **136**, 1803–1806.
61 S. Sonia, R. Jayasudha, N. D. Jayram, P. S. Kumar, D. Mangalaraj and S. Prabagaran, *Curr. Appl. Phys.*, 2016, **16**, 914–921.
62 R. Ruhal and R. Kataria, *Microbiol. Res.*, 2021, **251**, 126829.
63 L. B. Capeletti, J. F. A. de Oliveira, L. M. D. Loiola, F. E. Galdino, D. E. da Silva Santos, T. A. Soares, R. de Oliveira Freitas and M. B. Cardoso, *Adv. Funct. Mater.*, 2019, **29**, 1904216.
64 I. E. Mba and E. I. Nweze, *World J. Microbiol. Biotechnol.*, 2021, **37**, 1–30.
65 D. Li, S. Chen, K. Zhang, N. Gao, M. Zhang, G. Albasher, J. Shi and C. Wang, *Sci. Rep.*, 2021, **11**, 1703.
66 M. Zerouali, D. Bouras, R. Daira, M. Fellah, B. Boudjema, R. Barille, E.-F. Sakher, S. Bellucci and G. A. El-Hiti, *Opt. Mater.*, 2024, **152**, 115495.
67 P. P. Mahamuni-Badiger, P. M. Patil, M. V. Badiger, P. R. Patel, B. S. Thorat-Gadgil, A. Pandit and R. A. Bohara, *Mater. Sci. Eng. C*, 2020, **108**, 110319.
68 T. Popescu, C. O. Matei, I. D. Vlaicu, I. Tivig, A. C. Kuncser, M. Stefan, D. Ghica, L. C. Miclea, T. Savopol and D. C. Culita, *Sci. Rep.*, 2020, **10**, 18062.
69 B. Ahmed, F. Ameen, A. Rizvi, K. Ali, H. Sonbol, A. Zaidi, M. S. Khan and J. Musarrat, *ACS Omega*, 2020, **5**, 7861–7876.
70 G. Dutta, S. kumar Chinnaiyan, A. Sugumaran and D. Narayanasamy, *RSC Adv.*, 2023, **13**, 26663–26682.